Geophys. J. Int. (2005) **162,** 156–168 doi: 10.1111/j.1365-246X.2005.02652.x

Faulting geometry for the complex 1980 Campania-Lucania earthquake from levelling data

A. Amoruso, L. Crescentini and R. Scarpa

Department of Physics, University of Salerno, 84081 *Baronissi (SA), Italy. E-mail: antonella.amoruso@sa.infn.it*

Accepted 2005 March 31. Received 2005 January 10; in original form 2004 August 27

SUMMARY

The destructive 1980 Campania-Lucania earthquake was a complex event, consisting of at least three subevents. While the main features of the first (0 s) and of the last (40 s) subevents are widely accepted, the second subevent (20 s) is still controversial. Fault geometries are here determined from levelling data, using a global minimization technique. Even if uplifts of southernmost benchmarks (the most sensitive to the 20 s subevent) are small, new proper statistical analysis allows us to draw a few robust conclusions. Our results agree with previously accepted models as regards the 0 and 40 s subevents. As regards the 20 s subevent, previous models always assumed a northeast-dipping fault, while levelling data show that it could have been equivalently caused by a rupture dipping either southwest or northeast. The statistical significance of the two models is about the same, and strike and dip of the two faults are consistent with the two focal planes previously obtained from teleseismic data. Aftershock distribution seems to favour the southwest-dipping fault model.

Key words: Campania-Lucania earthquake, earthquake parameters, seismic deformations.

1 INTRODUCTION

The 1980 November 23 Campania-Lucania earthquake, also known as the Irpinia earthquake (surface wave magnitude $M_s = 6.9$, killing around 3000 people), was one of the most destructive earthquakes which occurred in Italy in the 20th century and was a relatively rare complex large normal faulting earthquake. Better knowledge of this event will contribute not only to an understanding of the active tectonics of Italy and the recognition of local active structures, but also to an understanding of extensional tectonics in general.

This earthquake was the first event in Italy for which sizeable and coherent surface faulting has been positively recognized, first by Westaway & Jackson (1984), who described a 10 km fault scarp, and later by Pantosti & Valensise (1990), who reconstructed a steeply dipping fault scarp extending from both ends up to 38 km total length. Recently, Blumetti *et al.* (2002) mentioned a further 8 km end-to-end rupture about parallel to the previous ones (Fig. 1). Inversion of teleseismic data allows us to state the main features of the earthquake, which was unanimously recognized as a complex event comprising at least the main shock and two subevents occurring about 20 and 40 s later (e.g. Westaway & Jackson 1987; Giardini 1993). Most published seismic moments range between 2.4×10^{19} and 3.0×10^{19} N m, fault dip for the main shock between 53° and 63° and strike between 305° and 330°.

Results from different data sets (teleseismic records, strong motion records, levellings, geological evidence) are in good agreement regarding the features of the fault related to the main shock (0 s subevent) and are similar regarding the 40 s subevent, but are in strong disagreement regarding the 20 s subevent.

The fault scarps recognized by Westaway & Jackson (1984) and the northern extension in Pantosti & Valensise (1990) are unanimously associated with the 0 s subevent. Localization of the main shock (Westaway & Jackson 1987) and of the 40 s subevent (Bernard & Zollo 1989) from seismic data is also generally accepted (e.g. Nostro *et al.* 1997).

The *P*-wave radiation of the 20 and 40 s subevents shows a very similar azimuthal distribution (Westaway & Jackson 1987). One nodal plane dips northeast at 20° and strikes −45°, the other nodal plane dips southwest at 70° and strikes 135°. Bernard & Zollo (1989) chose the 70° southwest-dipping plane as the fault plane for the 40 s subevent, mainly because of the aftershock mechanisms, the distribution of aftershocks and geological field observations. A more steeply dipping (about 85°) fault has been suggested by Pingue & De Natale (1993) from levelling data.

Westaway & Jackson (1987) showed that this fault plane solution for the 20 s subevent can account for the relative amplitudes and azimuthal distribution of the compressional pulses at about 25 s in the teleseismic records. The southwest-dipping plane is constrained by the large amplitude of compressional pulses at stations to the northeast and east of the epicentre. Bernard & Zollo (1989) chose the 20° northeast-dipping plane as the fault plane because of the observed subsidence on the southern part of the epicentral area and the concentration of aftershock activity beneath and to the east of San Gregorio Magno (hereinafter referred to as SGM), and associated the SGM fractures with the 20 s subevent through a secondary faulting system (see also Nostro *et al.* 1997). Pingue *et al.* (1993) checked several direct models against levelling data and suggested a much shallower (about 1 km deep) fault. All later papers share a

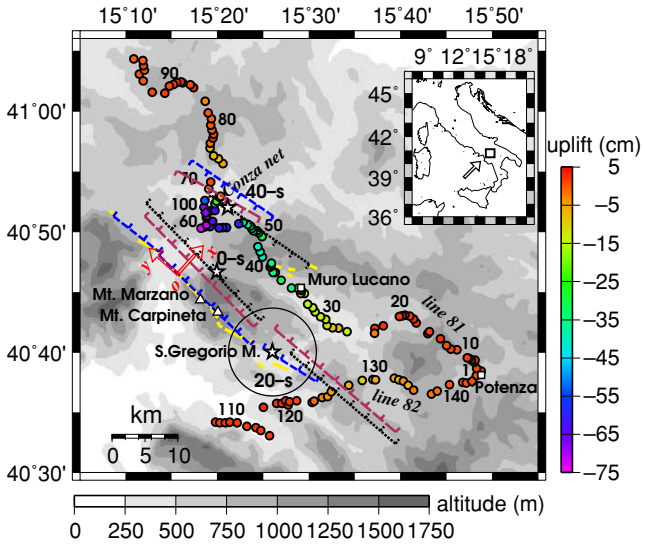

Figure 1. Map of the faulted area. Outlined circles, benchmark sites (labelled every 10) and uplifts; outlined diamonds, shared benchmarks; stars, subevent epicentres according to Westaway & Jackson (1987) (0 s), and Bernard & Zollo (1989) (20 and 40 s). The circle around the epicentre of the 20 s subevent is its estimated error according to Bernard & Zollo (1989). Thick solid lines west of line 81 indicate the fault scarps identified by Westaway & Jackson (1984) and Pantosti & Valensise (1990). Thick solid lines east of line 81 indicate the fault scarps identified by Blumetti *et al.* (2002). Surface projection of the upper side of the subevent source faults according to Bernard & Zollo (1989) (dotted), Pantosti & Valensise (1990) (dashed) and Pingue & De Natale (1993) and Pingue & De Natale (1993) (long-dashed) are also shown. Rotated axes (origin at 15°15′39″E, 40°46′31″N) have been used for inversions.

northeast-dipping fault. Relying mainly on surface fracture investigations, Pantosti & Valensise (1990) ascribed the SGM fractures to the 20 s subevent and suggested a source fault striking about −50° and dipping about 60° northeast—an extension of the fault responsible for the 0 s subevent. According to Pantosti *et al.* (1993a,b) the 0 and 20 s fault segments ruptured during four palaeoearthquakes which show essentially the same geometry and amount of released slip of the fault indicated to be responsible for the 20 s subevent.

Accelerograms at three stations located close to the epicentral area (AUL, BRI and TRI, see Fig. 1 in Bernard & Zollo 1989) show high accelerations very likely related to the 20 s subevent. They have been investigated, for example by Bernard & Zollo (1989) and Vaccari *et al.* (1993), to locate the 20 s source but, as stressed by Bernard & Zollo (1989) 'the first arrival *P* or *S* from this shock are not easy to identify on the three records (TRI, AUL, BRI) because of the high level of reverberated phases'. Moreover, timing is affected by uncertainties in the nucleation site of the main shock (which triggered the accelerometers) and in the velocity model. In agreement with Cocco & Pacor (1993a,b) we believe that the scarce source coverage does not allow us to extract more information on the source mechanism of the 20 s subevent. Localization of the 20 s subevent from seismic data in Westaway & Jackson (1987) is about 20 km northwest of that in Bernard & Zollo (1989) and of the SGM fractures.

Data with different types of resolution (accelerograms, teleseismic waveforms, surface fractures and geodetic data) are commonly jointly inverted, and *a priori* equal weights are often used (e.g. Salichon *et al.* 2003). In this work we prefer a different approach, performing a non-linear global inversion of levelling data and checking for the effects of the modelling assumptions (e.g. uniform slip distribution). If available geodetic data prove capable of distinguishing between different models, and results are fully consistent with results from all other data, not only can we confirm the reliability of geodetic data but we are also confident that results are not due to some kind of compromise. For example, when jointly inverting two data sets, a similar confidence could be reached using trade-off curves between the two terms of the cost function while varying the relative weights (e.g. Amoruso *et al.* 2002). In this work the huge number of free parameters (see Section 4) makes this procedure impractically long, but if available geodetic data turn out to be scarcely able to distinguish between different models, and/or results are not fully consistent with results from all other data, a joint inversion is necessary. We will see that this is not the case in this work.

The non-linear global inversion is performed following Amoruso *et al.* (2002), but here for the first time it is applied to a complex earthquake comprising three distinct events. Moreover, we have used a new approach to get residual statistics, assert statistical significance of competing models and investigate the resolving power of experimental data.

2 DATA SET

Precision levellings were carried out along lines 81 and 82 of the IGMI (Italian Military Geografic Institute) high-precision national levelling network before the earthquake in 1958 and 1959 and after the earthquake in 1981. The two lines share a benchmark near Potenza (Fig. 1). The field measurements were performed according to the criteria of high-precision levelling, i.e. $t = \pm 0.25\sqrt{L}$ cm, where t is the tolerance of the difference between the fore and back levelling between two subsequent benchmarks and L is the distance between the two benchmarks in kilometres. Actual measurement errors were probably lower, since closing errors were much smaller than expected (Arca & Marchioni 1983). Combined survey precision $t = \sqrt{t_{\rm pre}^2 + t_{\rm post}^2}$ depends on the precision of pre-earthquake and post-earthquake levellings; a conservative estimate based on above-mentioned tolerance limit is $t = \pm 0.35\sqrt{L}$ cm.

Further measurements were carried out at a small levelling network connected to line 81 (12 benchmarks near the Conza Dam, Fig. 1) in October 1980 and just after the earthquake (Cotecchia *et al.* 1986).

Our data set consists of measurements at 142 benchmarks: 98 benchmarks of line 81 (excluding the benchmark shared with line 82) 36 benchmarks of line 82 (including the benchmark shared with line 81), and eight benchmarks of the Conza Dam levelling network (excluding the benchmark connecting it with line 81). As regards lines 81 and 82, the data set is consistent with Pantosti & Valensise (1990), who inspected the most significant parts of line 81. We have not taken into account benchmarks of line 82 near Eboli (60 km west of Potenza), because they are located mostly on limestone outcrops and suffered a relevant subsidence from 1958 to 1981 (e.g. Fig. 12 in Pantosti & Valensise 1990) certainly not ascribable to the 1980 Campania-Lucania earthquake. Following Pingue *et al.* (1993) we have taken into account benchmarks close to the epicentral area (Figs 1 and 2) since the well-correlated subsidence of that part of line 82 can be reasonably considered as coseismic. Its amount with respect to the benchmark shared with line 81 (about 8 cm) is much larger than the cumulative measurement error (about 1.4 cm, from $L \approx 15$ km). The subsidence shows a quasi-symmetrical shape and the levelling line completely recovers from subsidence going on westward. Only three non-consecutive data

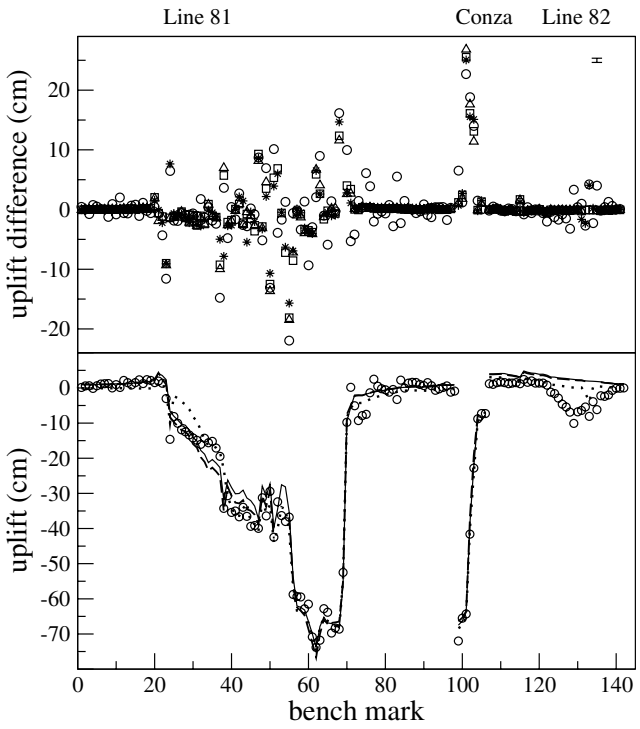

Figure 2. Top: Measured uplift differences between adjacent benchmarks (circles) and predicted values if all sections are M_2-inverted (squares), if most scattered sections are discarded (triangles), and if southern sections are M_1-inverted for the 20 s fault, after fixing the 0 and 40 s faults to their best-fit values obtained by inverting uplifts (stars). Section 69–70 is out of the frame. The error bar at the upper right corner of the plot represents a typical measurement error on uplift differences. Bottom: Observed uplifts along the levelling lines (circles); predicted uplifts if all sections are M_2-inverted (solid line), if most scattered sections are discarded (dashed lines), and if southern sections are M_1-inverted for the 20 s fault, after fixing the 0 and 40 s faults to their best-fit values obtained by inverting uplifts (dotted lines).

(129, 133 and 135 in Fig. 2) depart from the smooth pattern of benchmark vertical displacements, appearing as subsidence spikes and suggesting local soil compaction. Moreover, the reliability of line 82 is *a posteriori* checked for by inspecting its capability to resolve parameters of the 20 s subevent fault and their consistency with other data sets. As regards the Conza Dam line, not taken into account by Pantosti & Valensise (1990), we follow Pingue & De Natale (1993). Benchmarks are numbered starting from line 81, south to north, continuing on the Conza Dam network, and on line 82, west to east (Fig. 1).

3 MODELLING

The 1980 Campania-Lucania earthquake is generally considered to comprise three main normal-faulting subevents. Here we assume that the source faults are rectangular, slip is homogeneous on each fault, and faults are embedded in a homogeneous elastic half-space (Okada 1985). The complete formulation of faulting for each fault involves strike, dip and rake angles, magnitude of the slip vector, two geometrical dimensions, depth of the fault upper side and position of the centre of the fault trace. For three distinct faulting events, modelling depends on 27 parameters. Faults 1 and 2 (the 0 and 40 s faults of the literature) are located in the northern part of the epicentral area and fault 3 (the 20 s fault) is located in the middle and southern parts of it.

Several tests indicate that a totally unconstrained inversion of levelling data is scarcely reliable as regards the location of the 0 s subevent, which appreciably affected benchmarks running almost parallel with its source fault. The main features of the 0 s subevent are, however, well constrained by the surface ruptures along the Mount Marzano and Mount Carpineta segments (Fig. 1) and by seismic data, so we fix strike (N48W) and dip (60°) of the 0 s fault and we let the fault trace move along the above-mentioned fractures. To meet this constraint easily, we use a coordinate system where the x-axis strikes N42E and the y-axis strikes N48W. The axis origin is located at 15°15′39″E, 40°46′31″N (Fig. 1). In what follows, strike is given in degrees clockwise from the y-axis, when it is not specified in terms of the cardinal points. Because numerical tests indicate that rake angles are scarcely resolved by available levelling data, we assume a pure normal faulting mechanism for all the sources, consistently with seismic data from the Irpinia earthquake and with regional seismicity, and as always accepted in the literature. These constraints reduce the number of free parameters to 21.

The effects of the assumptions (uniform slip distribution, planar faults, homogeneous half space, etc.) on results will be discussed later in the text, and we will see that all relevant features are unaffected.

4 INVERSION TECHNIQUE

Data inversion leads to minimizing a cost function which measures the disagreement between model and observations adjusting a suitable set of model parameters. The cost function is obtained from maximum-likelihood arguments according to the statistical distribution of the residuals, i.e. of the differences between data and model predictions (Amoruso *et al.* 1998, 2002). We use two different cost functions, namely the mean squared deviation of residuals (chi-square fitting, M_2) and the mean absolute deviation of residuals (M_1). The cost function M_1 is less sensitive to the presence of outliers, which can prevent accurate determination of model parameters if M_2 is minimized (e.g. Press *et al.* 1992; Amoruso *et al.* 2002).

Residuals are due to random measurement errors as well as to non-measurement errors, mainly caused by interseismic and coseismic benchmark instabilities and the use of an inadequate model. As an example, we do not take into account curved faults, heterogeneities in the elastic properties of the medium, local response effects like soil compaction, landslides, topographic focusing, etc.

In the case of levelling surveys, random measurement errors depend on the square root of the distance between consecutive benchmarks, and generate a white Gaussian noise on section height differences and a random-walk noise on uplifts, since height differences between adjacent benchmarks are statistically independent experimental data (Arnadottir *et al.* 1992; Murray *et al.* 1996).

Non-measurement errors are often uncorrelated. Their distribution is not Gaussian and is possibly asymmetrical (e.g. because of soil compaction). They can generate a high-frequency noise with a wavelength comparable to benchmark spacing. Sometimes non-measurement errors largely exceed measurement errors, particularly if benchmark spacing is short.

Both measurement and non-measurement errors always affect the residuals. When using a covariance matrix including only measurement errors (e.g. Arnadottir *et al.* 1992), it is implicitly assumed that uncorrelated non-measurement errors are negligible. It has already

been noted that when uncorrelated errors are neglected results can appear biased towards fitting a few locally extreme values of the slope of the levelling curve at the expense of smoother trends in the levelling data, which should be the more robust features of the signal (Pollitz *et al.* 1998). Decimating levelling data could help in reducing the bias, but it is intrinsically affected by spatial aliasing. In order to take into account both measurement and non-measurement errors in a χ^2 fitting, the data covariance matrix has to include both off-diagonal and diagonal terms (e.g. Pollitz *et al.* 1998, for post-seismic benchmark instability).

Measurement errors can be easily estimated, while non-measurement errors are usually scarcely known. The relative importance of the two kinds of error can be stated using model stability analysis, but in this work such a procedure is computationally too intensive. Here we use a simple test to check whether measurement or non-measurement errors dominate. If errors are normally distributed, the ratio χ^2/g between the total square residual for the χ^2 best-fit model and the number of degrees of freedom (g) is a good statistical estimate of the *a priori* scaling of the uncertainties. At first we use section height differences as statistically independent data, and assign the conservative estimate $0.35\sqrt{L}$cm (see Section 2) to measurement errors. We then compute χ^2/g for the best-fit model. If $\chi^2/g \approx 1$ than measurement errors can account for the misfit between data and predictions, but if $\chi^2/g \gg 1$ than non-measurement errors account for the misfit. In this latter case it can be appropriate, even if not rigorous, to neglect measurement errors.

The cost function that we minimize for normally distributed residuals is

$$\mathcal{M}_2 = \sum_{j=1}^{3} \sum_{i=1}^{N_j} \left(\frac{v_{ji} + u_0 - \overline{v}_{ji}(\mathbf{a})}{\sigma_{ji}} \right)^2 . \quad (1)$$

The cost function for two-sided-exponential distributed errors is

$$\mathcal{M}_1 = \sum_{j=1}^{3} \sum_{i=1}^{N_j} \left| \frac{v_{ji} + u_0 - \overline{v}_{ji}(\mathbf{a})}{\sigma_{ji}} \right| . \quad (2)$$

In the case of negligible measurement errors, v_{ji} is the coseismic uplift of benchmark i, line j, $N_1 = 98$ (benchmarks from line 81), $N_2 = 8$ (Conza Dam net) and $N_3 = 36$ (benchmarks from line 82). Static baseline correction u_0, common to the three linked nets, behaves like a further free parameter of the model. In the case of negligible non-measurement errors, v_{ji} is the coseismic change of section height difference i, line j ($j = 1, 2, 3$), $N_1 = 98$ (levelling sections from line 81), $N_2 = 8$ (levelling sections from the Conza Dam net) and $N_3 = 35$ (levelling sections from line 82). Static baseline correction is removed. Model predictions $\overline{v}_{ji}(\mathbf{a})$ depend on model parameters $\mathbf{a}$.

The reliability of the best-fit model can be tested through its sensitivity to the assumed error distribution and checking the *a posteriori* distribution of residuals against the assumptions.

Minimizing the cost function requires the use of numerical techniques capable of finding the global minimum in the presence of multiple local minima, whose number and depths are increased by experimental noise. We use the ASA (adaptive simulating annealing) method (e.g. Ingber & Rosen 1992; Ingber 1993) which is able to self-optimize its own cooling parameters recursively. Success in finding the global minimum is never guaranteed, but we believe that it is more important to identify the region of parameter space that contains models of acceptable data fit. This is accomplished by running a large number of inversions with random initial cooling parameters starting from random points of the parameter space. Endpoints are then plotted versus related costs.

To increase reliability of the global inversion results, we use a two-step procedure. First, we run tens of inversions, starting from different initial points of the parameter space and using different initial values of the cooling parameters. Parameter bounds regarding fault locations are very large and rely on the assumption that faults 1 and 2 (the 0 and 40 s faults of the literature) are located in the northern part of the epicentral area, and fault 3 (the 20 s fault) is located in the middle and southern parts of it. No bound is given to strike and dip of faults 2 and 3, or to depth, dimensions or slip magnitude of all the faults. Parameter values are allowed to vary in discrete steps. Computed values of model parameters and of costs are then used to tighten the bounds of better-resolved parameters for the latter step, where all parameters are allowed to vary continuously. The procedure reduces the volume of the sampled parameter subspace for this latter set of inversions, thus increasing optimization efficiency.

Because of correlation between different parameters, number of parameters and unknown distribution of residuals, determination of the confidence intervals is a quite difficult task. The bootstrap percentile method applies the best-fit technique to a large number of synthetic data sets, obtained by randomly resampling from the actual data set with replacement, and is often used to estimate confidence intervals without making assumptions about the underlying statistics of the errors (e.g. Arnadottir & Segall 1994). Bootstrapping also allows estimate correlations between different parameters, by forming a scatter plot of all the estimates for each parameter pair and visualizing the correlations between the parameter pairs (for details see Cervelli *et al.* 2001).

Strictly speaking, a full optimization procedure should be performed at each resample, but in our case computation time would be unacceptable. In this work we use a faster method (downhill simplex, Press *et al.* 1992), starting from selected models to explore the parameter region surrounding each faulting model. We will see that global inversion of levelling data produces two well-defined minima in two very different regions of the parameter space or, in other words, leads to two very different faulting models. We use these two models as starting points for downhill simplex minimization of the misfit between predictions and bootstrapped data. Separate analysis of the two models is possible because the downhill simplex technique is able to explore the regions related to the two models, but unable to jump from one region to the other.

This approach allows us not only to determine confidence intervals of model parameters but also to state the statistical significance of the cost difference between competing models.

5 INVERSION RESULTS

First we minimize cost function M_2 using section height differences as statistically independent data. The data set includes sections connecting line 81 to line 82, and the Conza net to line 81. Using $\sigma_i = 0.35\sqrt{L_i}$ cm, where L_i is the distance in kilometres between two consecutive benchmarks, the best-fit χ^2 is 10751, g is 120 (141 levelling sections minus 21 free fault parameters) and χ^2/g is 89.6 ($\gg 1$). In order to reduce the effects of the most scattered data, we exclude the 10 sections whose residuals divided by $\sigma_i = 0.35\sqrt{L_i}$ are larger than twice the standard deviation ($2\sqrt{\chi^2/141}$). The best-fit χ^2 is now 5616, g is 110, and χ^2/g is 51.1, again $\gg 1$.

The conclusion that measurement errors cannot account for misfit is also supported by comparison between predicted and observed deformation patterns. The best-fit model scarcely reproduces data for line 81 and is completely unable to reproduce the subsidence of

line 82 (in particular benchmarks 120 to 138), even after excluding from the data set those data whose residuals exceed twice the standard deviation (Fig. 2). Similar results have been obtained minimizing M_1, both using all data or only data which see the 20 s subevent (benchmarks 1–35 on line 81 and 107–142 on line 82). In this latter case we have subtracted the contribution to vertical displacements by the 0 and 40 s faults, whose parameters (models A and B, see later in this section) have been obtained by inverting uplifts (Fig. 2).

Since non-measurement errors largely exceed measurement errors, considering benchmark uplifts as statistically independent data appears adequate. This conclusion is supported by a systematic general study of the effects of error treatment in the inversion of levelling data using model stability analysis (Amoruso *et al.*, in preparation). As already mentioned, such a procedure is computationally too intensive in the case of the Campania-Lucania earthquake. We have performed a small number of tests taking into account combined (measurement and non-measurement) errors. Non-measurement errors have been assumed small (with respect to measurement errors) where benchmarks were slightly affected by the earthquake, and large where benchmarks were strongly affected by the earthquake and uplift values are very scattered. Results are quite similar to those obtained assuming negligible measurement errors everywhere.

We have run hundreds of inversions considering uplifts as statistically independent data and minimizing M_1 and M_2. Uncertainties σ_{ji} could be different from one another, but we assign the same uncertainty to all uplifts. For the sake of simplicity, we put $\sigma_{ji} = 1$ cm for all data, since using a different value leads to a mere misfit scaling. Several tests indicate that results are scarcely affected by the choice of assigning the same uncertainty to all uplift data.

We have checked the *a posteriori* residual distribution from each inversion against the assumed distribution (Gaussian or two-sided exponential) using the standard Kolmogorov–Smirnov and Kuiper tests on cumulative distributions (e.g. Press *et al.* 1992). The Kolmogorov–Smirnov test tends to be most sensitive around the median value and less sensitive at the extreme ends of the distribution, while the Kuiper test guarantees equal sensitivities at all values of the residuals. Since the cost function M_2 has undesired sensitivity to outlying points, the *a posteriori* distribution of residuals should be checked against the assumed distribution using a test which is most sensitive at the extreme ends of the distribution, but unfortunately there is no suitable simple test applicable to unbinned distributions (Press *et al.* 1992). The Kolmogorov–Smirnov and the Kuiper tests tend to underestimate the statistical significance of the presence of outlying points, thus overestimating the consistency of residuals with a Gaussian distribution function, with respect to reality.

According to the Kolmogorov–Smirnov (Kuiper) test, the *a posteriori* residual distribution is consistent with a two-sided-exponential distribution at more than the 95 per cent significance level for 47 per cent (49 per cent) of the M_1 minimizations, and the median of the significance level is 94 per cent (95 per cent). On the other hand, according to the Kolmogorov–Smirnov (Kuiper) test the *a posteriori* residual distribution is consistent with a Gaussian distribution at more than the 95 per cent significance level for 1 per cent (9 per cent) of the M_2 minimizations, and the median of the significance level is 76 per cent (76 per cent). We have also minimized M_2 after excluding data whose residuals are larger than twice the standard deviation (all belonging to line 81), but results are quite similar to those obtained using all data.

Because residual distribution is much more consistent with a two-sided-exponential distribution than with a Gaussian distribution, and model parameters obtained when minimizing M_1 and M_2 differ in details only, for the sake of conciseness and clarity we are going to show only those results obtained when minimizing M_1. As previously mentioned, a few spikes, possibly due to local soil compaction, are quite evident in the uplift pattern. When minimizing M_1 the effects of these outliers are greatly damped. Comparisons with M_2 minimization will be discussed only when they are interesting.

The presence of two shallow antithetic faults in the northern part of the epicentral area, in agreement with previously published models, is a common feature of all inversions. As regards fault 3 (the 20 s subevent), Fig. 3 shows values of strike and dip obtained by the minimization procedure. Strike values are concentrated into two narrow intervals around -10° (circles) and 170° (stars). Related dip values are concentrated into two narrow intervals around 25° and 65° respectively. The former kind of solution (hereafter referred to as A) gives a fault dipping at a low angle towards the northeast and located close to SGM. The latter kind of solution (hereafter referred to as B), gives a fault dipping at a higher angle towards the

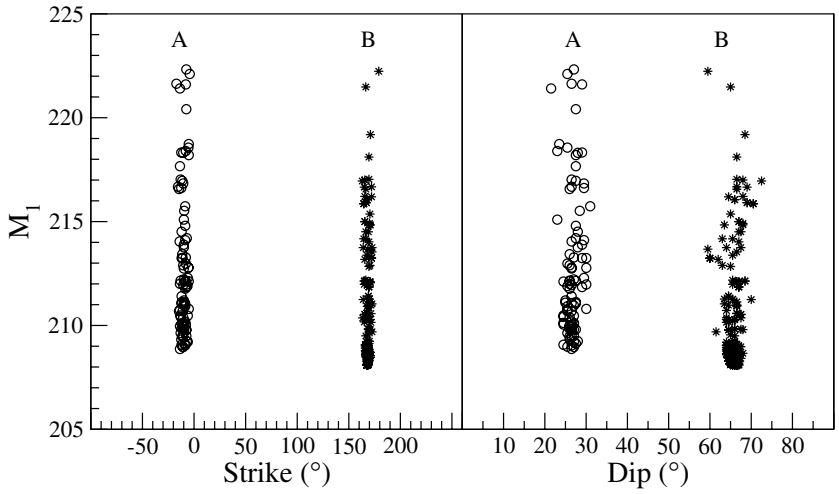

Figure 3. Values of strike (left panel, degrees clockwise from the *y*-axis of Fig. 1) and dip (right panel) of the 20 s fault from all the inversions performed minimizing M_1. Note that steeply dipping faults always strike about N120E while low-angle dipping faults always strike about N60W.

southwest and located close to Muro Lucano. Each unconstrained inversion gives a model which unambiguously belongs to either A or B. To obtain variabilities of the 21 parameters, we have sorted the N inversions related to each solution with respect to each parameter and considered the value of the same parameter in inversion number $0.5 \times N$ and in inversion number $0.95 \times N$. The variability of parameters for the two solutions and best-fit values are listed in Table 1. The 20 s fault planes obtained from geodetic data are quite similar to those obtained by Westaway & Jackson (1987) from teleseismic records.

Since the 20 s subevent is seen by few benchmarks (1–35 on line 81, which from number 22 also see the 0 s subevent, and 107–142 on line 82), it might look strange that two well-defined minima of strike can be obtained. We have thus minimized M_1 using all data, after fixing the strike of the 20 s subevent at different values from 0° to 360°, and optimizing the other 20 parameters. Fig. 4 shows costs computed using displacements at all benchmarks (left plot) and at benchmarks 1–35 and 107–142 (right plot). The two minima are well defined, and the left plot can be approximately obtained by shifting the right plot upwards, thus proving not only that data are able to constrain the strike of the 20 s subevent but also that cost differences are essentially ascribable to benchmarks 1–35 and 107–142. Fig. 4 also prove the resolving power of levelling data with respect to the 20 s fault.

Table 1. Best-fit model parameters and range of variability when minimizing M_1.[a]

Parameter	A (NE-dipping fault)		B (SW-dipping fault)	
	Best-fit value	Range of variability	Best-fit value	Range of variability
Fault 1 (0 s subevent)				
X (km)	0.0	Fixed	0.0	Fixed
Y (km)	−1.8	−2.4 to −1.3	−2.2	−2.5 to −1.6
Z (km)	2.5	0.7–2.5	0.2	0.1–2.1
Length (km)	25.0	23.0–25.7	24.0	23.1–25.4
Width (km)	11.3	11.0–13.5	13.6	11.7–14.0
Strike[b] (°)	0	Fixed	0	fixed
Dip (°)	60	Fixed	60	Fixed
Rake (°)	−90	Fixed	−90	Fixed
Moment[c] (10^{18} N m)	21.6	21.4–22.5	26.1	22.5–26.2
Fault 2 (40 s subevent)				
X (km)	12.2	12.0–12.3	12.2	12.0–12.3
Y (km)	2.9	2.8– 4.6	2.8	2.7–4.6
Z (km)	1.8	1.6–1.9	1.7	1.5–1.8
Length (km)	16.6	16.2–19.9	16.6	16.5–20.0
Width (km)	1.0	1.0–2.2	1.2	1.0–2.2
Strike[b] (°)	170.1	169.0–170.4	170.0	169.1–170.5
Dip (°)	73.4	70.5–77.2	72.0	71.4–76.1
Rake (°)	−90	Fixed	−90	Fixed
Moment[c] (10^{18} N m)	1.2	1.2–1.3	1.2	1.1–1.8
Fault 3 (20 s subevent)				
X (km)	−8.8	−9.6 to −6.3	14.0	13.3–14.4
Y (km)	−29.2	−29.5 to −27.4	−24.3	−25.2 to −23.1
Z (km)	8.7	7.2–9.2	7.5	5.7–8.2
Length (km)	20.8	18.0–22.2	20.2	18.7–22.8
Width (km)	2.6	2.0–6.6	6.2	2.2–9.7
Strike[b] (°)	−13.4	−14.0 to −5.1	168.2	165.2–171.4
Dip (°)	26.4	24.3–30.0	66.5	64.0–68.6
Rake (°)	−90	Fixed	−90	Fixed
Moment[c] (10^{18} N m)	2.4	2.4–2.5	2.7	2.4–2.8

[a]Range of variability obtained by sorting the N inversions related to each solution with respect to each parameter and considering the value of the same parameter in inversion number $0.5 \times N$ and in inversion number $0.95 \times N$. Axis origin at 15°15′39″E, 40°46′31″N; x-axis strikes N42E; y-axis strikes N48W.
[b]Clockwise from y-axis.
[c] $\mu = 3 \times 10^{10}$ N m^{-2}.

The along-dip width of fault 2 (the 40 s subevent) is always unreasonably small. This feature could be forced by the large uplift scatter in the small region of maximum subsidence (Figs 1 and 2), which cannot be well reproduced by a uniform-slipping fault, and may focus the slipping area close to the surface. When larger values of the along-dip width are forced, cost increases but measured and predicted subsidence still compare well; parameters of the other faults are not affected appreciably. After a few tests, we have set the lower bound of along-dip width of fault 2 equal to 1 km just for computation purposes.

Comparison between predicted and measured uplifts for A and B is shown in Fig. 5. Even if the two models are very different as regards the 20 s subevent, they provide nearly indistinguishable data fits. Odd moments of the *a posteriori* residual distributions are negative, supporting the existence of benchmarks which suffered anomalous subsidence.

From Cervelli *et al.* (2001), we use bootstrapping to draw covariance scatter plots and *a posteriori* distributions of the model parameters. In our case, two and only two well-resolved regions of cost minima (related to A and B) exist in the parameter space. To analyse the two models, we generate 5000 synthetic data sets using bootstrapping and we invert them for all 21 model parameters using each of the two best-fit minima as the starting point and downhill simplex as the minimization technique.

Figs 6 and 7 show results obtained for parameters of fault 3 (the 20 s subevent), starting from the best-fit model A and B respectively. The most evident correlations are between y-position and fault length for both models, fault length and moment for A, and fault depth and moment for B. No clear correlation between parameters of different faults is evident in appropriate covariance scatter plots. The *a posteriori* distribution of the parameters (bottom row) is used to evaluate confidence intervals. Median and 95 per cent confidence intervals for fault parameters (A and B) are listed in Table 2. Note that medians are very close to best-fit values. Fig. 8 shows cost cumulative distribution after inverting bootstrapped data starting from models A and B. Even if the best-fit cost of B is a little lower than best-fit cost of A, cost distributions are undistinguishable for M_1 and only slightly different for M_2. Consequently, A and B are statistically almost equivalent.

The surface projections of the faults of best-fit A and B and associated vertical displacements are shown in Fig. 9.

6 EFFECTS OF MODELLING ASSUMPTIONS

6.1 Flat surface

Armigliato & Tinti (2003) investigated the perturbations introduced by the local topography on the coseismic displacement components induced by the 0 s northeast-dipping normal fault proposed by De Natale *et al.* (1988) and Pingue *et al.* (1993), using a 2-D approach. As regards vertical displacements, they found a satisfactory fit with the homogeneous half-space solution computed for a reference flat level coinciding with the average topography over a small distance containing the fault surface projection. In practice, this implies a possible error of tens of metres in fault depth (which of course is given with respect to local altitude and not to the mean sea level). There is no reason to expect different results when using our faults.

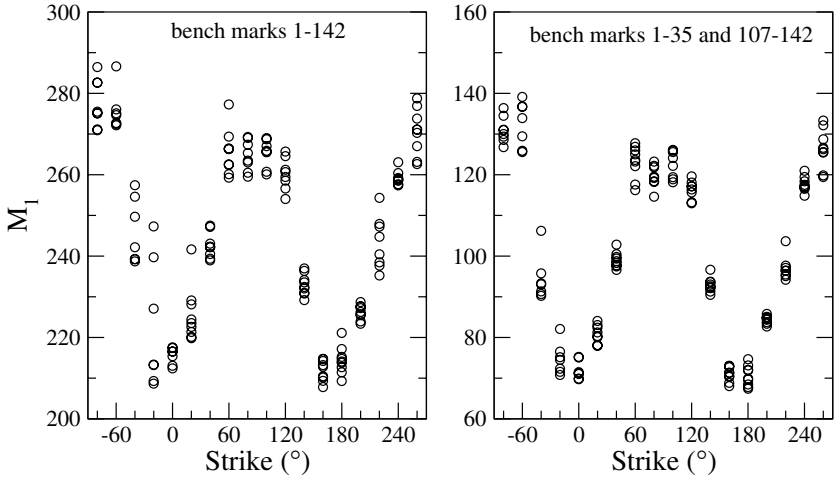

Figure 4. Cost M_1 for fixed values of the strike of the 20 s subevent (clockwise from the *y*-axis of Fig. 1); 20 parameters are free in the inversions. Left: Cost computed using vertical displacement at all benchmarks. Right: Cost computed using vertical displacement at benchmarks 1–35 and 107–142, i.e. the most affected by the 20 s subevent.

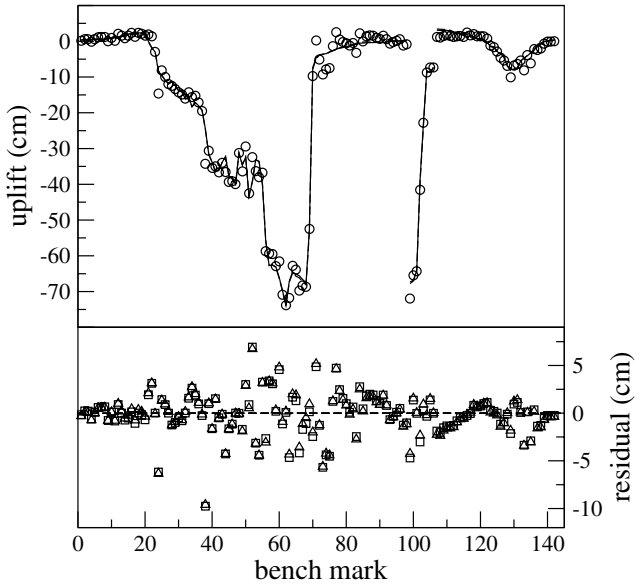

Figure 5. Top: Observed uplifts along the levelling lines (circles); predicted uplifts from best-fit A (dashed line) and best-fit B (solid line), after minimizing M_1. Bottom: Residuals from A (triangles) and B (squares). The fit to data is about the same for both models.

6.2 Homogeneous half-space

We have used the EDGRN/EDCMP 3-D code (Wang *et al.* 2003) to compute vertical displacements at all benchmarks, using both A and B models and the layered medium in Table 3. The two synthetic data sets have then been inverted as is done with experimental data. Optimal parameters are about the same as in models A and B, thus proving that crustal layering is not important in this case. Of course we cannot completely exclude effects from lateral heterogeneities, but it is reasonable to expect that they also cannot substantially modify the whole picture, since lateral *P*-velocity anomalies are of the order of a few per cent (Amato & Selvaggi 1993).

6.3 Planar faults

We have divided the 0 s fault into a shallower vertical segment (starting from the surface down to 5 km) and a deeper 60°-dipping segment (starting from 5 km depth) as suggested by Amato & Selvaggi (1993). Cost M_1 has been minimized using 20 free parameters, because the depth of the upper side of the deeper part of the 0 s fault is fixed. The main features of the model do not change, but cost increases to 225 for A-class inversions and to 237 for B-class inversions.

We have also tested a non-planar northeast-dipping 20 s fault consisting of a shallower vertical segment (starting from the surface down to a free depth z) and a deeper free-dipping segment (starting from z) (Bernard & Zollo 1989; Nostro *et al.* 1997). Cost M_1 has been minimized using 21 free parameters. The only noticeable differences with respect to results obtained for model A using planar faults are a larger width (about 13 km for the deeper part) and a smaller slip (about 20 cm) of the 20 s fault. Depth z is about 4.3 km. The cost increases to 227 if considering all data and to 79 if considering only benchmarks 1–35 and 107–142 (the cost for the same benchmarks is 65 for model A).

6.4 Uniform slip distribution

We partially relax the uniform slip assumption by dividing the 0 s and 20 s faults into a small number of coplanar subfaults. Rake is kept fixed (−90°), but slip magnitude is allowed to vary independently in each subfault (Amoruso *et al.* 2002).

The 0 s fault has been divided into three equal-length subfaults along strike, thus increasing the number of free parameters to 23. Optimal parameters are quite similar to those obtained using a uniform-slipping 0 s fault (A and B) and costs are, as expected, slightly lower (208 for A and 205 for B). Seismic moment release is distributed in percentages of approximately 38, 24 and 38 per cent among the three 0 s subfaults, consistently with the discontinuity in the surface faulting occurred in the Sele Valley (Pantosti & Valensise 1990) and with the slip-velocity distribution obtained from the analysis of strong-motion data (Cocco & Pacor 1993a,b).

The 20 s fault has been divided into four equal-sized subfaults (two along strike and two along dip), thus increasing the number of free parameters to 24. Once again optimal parameters are quite similar to those obtained using a uniform-slipping 20 s fault (A and B) and costs are slightly lower (208 for A and 204 for B). As expected, the 20 s fault size is less defined than in the uniform slip

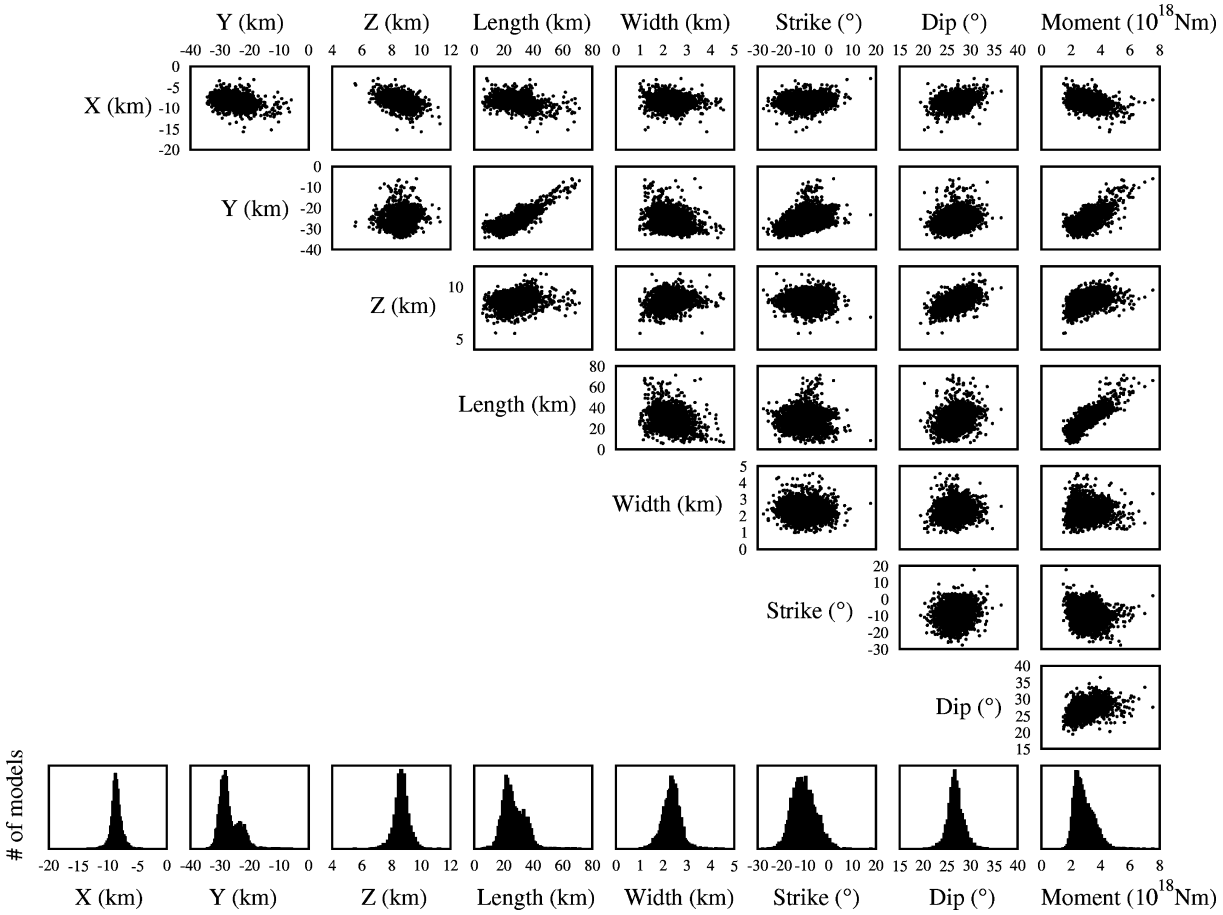

Figure 6. Covariance scatter plot for the 20 s fault of best-fit A, after minimizing M_1. The bottom row shows the *a posteriori* distribution of the parameters and allows their confidence intervals to be obtained. The other rows show correlations between parameter pairs.

model, but slip is mainly released where predicted by the uniform slip model.

7 COMPARISONS

7.1 Previous models

Fits to levelling data, line 82, from the model by Bernard & Zollo (1989) are shown in their Fig. 14(b). Fits to levelling data from the model by Pingue *et al.* (1993) are shown in their Fig. 2b. Pingue *et al.* (1993) also compared levelling data with vertical displacements computed with the fault model proposed by Pantosti & Valensise (1990) showing large discrepancies along both lines 81 and 82 (Fig. 6 in Pingue *et al.* 1993).

The model proposed by Pantosti & Valensise (1990) had not been optimized with respect to levelling data. Thus, in order to check for the actual capability of that kind of model to account for measured coseismic displacements, we have inverted benchmark uplifts letting fault parameters vary in narrow ranges (a few kilometres and a few degrees) around those given by Pantosti & Valensise (1990). The 20 s fault has been divided into four subfaults (two along strike and two along dip, with freely variable slip) to reduce the effects of the assumption of uniform slip distribution. Even so, best-fit cost is 299 for all benchmarks and 145 for benchmarks 1–35 and 107–142, which see the 20 s subevent. Slip is null in shallower subfaults and 88 and 98 cm in deeper subfaults, whose upper side is 7.4 km in depth. We can conclude that a northeast-dipping fault dipping at about 60° is unable to account for observed uplifts even relaxing the uniform slip assumption, and in any case slip would be released only at depth.

The 20 s fault proposed by Bernard & Zollo (1989) is similar to A, apart from fault width (15 to 20 km). However, they roughly estimated fault width inferring slip (30 cm) from subsidence of line 82, and using the seismic moment calculated by Westaway & Jackson (1987) from teleseismic records. Consistency with levelling data of the coexistence of a shallower steeper subfault and a deeper subhorizontal subfault has already been discussed in the preceding section.

The 20 s fault model by Pingue *et al.* (1993) was obtained from levelling data by a forward approach, and has recently been used to study post-seismic deformations (Dalla Via *et al.* 2003). We have tested an optimized (with respect to levelling data) model by inverting levelling data while letting fault parameters vary in a narrow range (a few kilometres and a few degrees) around those given by Pingue *et al.* (1993). The best-fit cost is 231 for all benchmarks and 76 for benchmarks 1–35 and 107–142.

Computed uplifts and observations for benchmarks 1–35 and 107–142 are shown in Fig. 10.

7.2 Aftershock distribution

We have investigated the spatial distribution of aftershocks by using data from the ENEL seismic stations (e.g. Fig. 1 in Bernard & Zollo

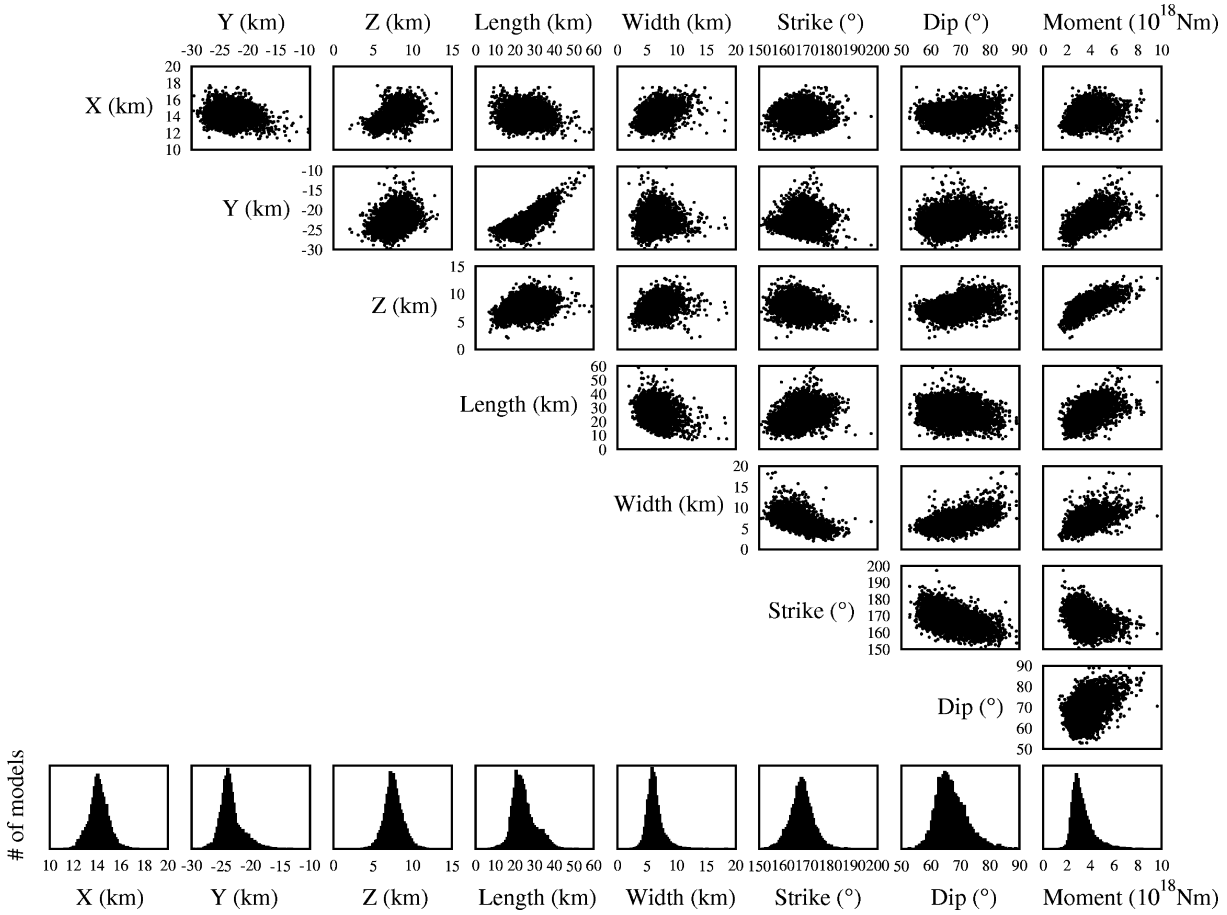

Figure 7. Covariance scatter plot for the 20 s fault of best-fit B, after minimizing M_1. The bottom row shows the *a posteriori* distribution of the parameters and allows their confidence intervals to be obtained. The other rows show correlations between parameter pairs.

1989) and from a temporary seismic network (up to 32 stations, e.g. Fig. 2 in Amato & Selvaggi 1993) deployed soon after the November 23 earthquake by Gruppo di Lavoro Sismometria and mainly operating from December 1 to 15. The data set, spanning from 1980 November 23 to 1981 October 31 and based on the analysis of all *P*- and *S*-wave arrivals, includes 26 796 *P*-wave arrivals, 8041 *S*-wave and 5087 *P*-wave polarities, corresponding to 2884 aftershocks. We have located hypocentres by using the HYPO71 code (Lee & Valdes 1985), and selecting events recorded by at least 10 stations (both *P* and *S* readings) with RMS value less than 0.4 s, horizontal uncertainty less than 3 km and depth uncertainty less than 5 km. The 1-D velocity model has been computed by using the VELEST algorithm (Kissling *et al.* 1994). Fig. 11 shows a vertical N31E cross-section cutting across the SGM area, including the profile of the 20 s faults of models A, B, Bernard & Zollo (1989), Pingue *et al.* (1993) and Pantosti & Valensise (1990), and hypocentres of the aftershocks localized southeast of the AA′ trace in Fig. 9. Aftershocks occurred in the hangingwall block of the 20 s fault of model B (as expected for normal faulting), but in the footwall block of the 20 s fault of any other model. This distribution is consequently more consistent with model B than with any other model. Occurrence of the aftershocks in the hangingwall of a possible northeast-dipping fault implies a big fault shift toward the southwest, inconsistent with coseismic deformations and surface fractures.

Using the 3-D tomographic simultaneous inversion method of Benz *et al.* (1996) the aftershock hypocentre pattern changes slightly, but the above-stated conclusion still holds.

8 DISCUSSION

The 20 s subevent is the most controversial among those constituting the 1980 Campania-Lucania earthquake. Our analysis of levelling data gives two models (A, low-angle northeast-dipping fault, and B, steep southwest-dipping fault) which are statistically equivalent, but the southern aftershock distribution is more consistent with model B. Model A is quite similar to the model of Bernard & Zollo (1989), and its 20 s fault is separated from the 0 s fault by an area lacking surface fracture.

The southern edge of the 0 s fault is always (A and B) very close to the southern end of the fractures north of SGM and is consistent with location of the 1996 ($M_L = 4.9$) earthquake (Fig. 9 and Cocco *et al.* 1999). The 20 s faults (A and B) end north of line 82, consistent with the presence of a different seismotectonic domain related to the 1857 earthquake south of line 82 (Pantosti & Valensise 1990), and with southern lowering of aftershock activity (Bernard & Zollo 1989). The location and length of the 20 s faults (A and B) are consistent with the estimates by Bernard & Zollo (1989) from strong-motion records and, as regards location, also with estimates by Westaway & Jackson (1987) from teleseismic data, whose uncertainty, according to Bernard & Zollo (1989), is greater than 20 km.

The 20 s faults (A and B) are deep, consistent with a suggestion by Westaway (1993) that the relatively low ground acceleration of this event (with respect to its seismic moment) could be associated with a relatively slow downward propagation of the rupture into the uppermost lower crust. The best-fit fault is narrow (especially A), but,

Table 2. Median and 95 per cent confidence intervals (CI) from bootstrapping when minimizing M_1.[a]

	A (NE-dipping fault)		B (SW-dipping fault)	
Parameter	Median	95 per cent CI	Median	95 per cent CI
Fault 1 (0 s subevent)				
X (km)	0.0	Fixed	0.0	Fixed
Y (km)	−1.4	−2.7–0.5	−1.9	−2.9–0.0
Z (km)	2.5	2.1–3.0	0.2	0.1–0.5
Length (km)	24.6	21.0–28.4	24.0	21.2–27.7
Width (km)	11.4	10.4–12.1	13.7	12.6–14.4
Strike[b] (°)	0	Fixed	0	Fixed
Dip (°)	60	Fixed	60	Fixed
Rake (°)	−90	Fixed	−90	Fixed
Moment[c] (10^{18} N m)	21.4	18.4–24.6	26.3	23.2–29.9
Fault 2 (40 s subevent)				
X (km)	12.2	11.9–12.4	12.2	12.0–12.4
Y (km)	3.0	2.1–4.5	3.0	2.2–4.2
Z (km)	1.7	1.3–2.2	1.7	1.3–2.1
Length (km)	17.1	14.6–22.6	17.0	14.6–21.1
Width (km)	1.0	1.0–1.2	1.2	1.0–1.5
Strike[b] (°)	169.8	167.7–171.9	169.9	167.7–171.9
Dip (°)	74.3	65.4–82.6	73.1	65.2–80.9
Rake (°)	−90	Fixed	−90	Fixed
Moment[c] (10^{18} N m)	1.2	0.9–1.9	1.2	0.9–1.8
Fault 3 (20 s subevent)				
X (km)	−8.6	−10.5 to −6.6	14.1	12.5–15.7
Y (km)	−27.8	−31.5 to −19.6	−23.7	−26.3 to −18.6
Z (km)	8.7	7.6–9.6	7.6	5.4–10.0
Length (km)	25.5	15.1–41.5	23.5	15.3–37.7
Width (km)	2.3	1.6–3.1	6.1	4.2–9.6
Strike[b] (°)	−10.7	−19.1 to −0.2	167.9	158.4–177.7
Dip (°)	26.8	23.5–30.4	66.3	58.7–79.0
Rake (°)	−90	Fixed	−90	Fixed
Moment[c] (10^{18} N m)	2.8	2.0–4.4	3.1	2.2–5.6

[a]Axis origin at 15°15′39″E, 40°46′31″N; x-axis strikes N42E; y-axis strikes N48W.
[b]Clockwise from y-axis.
[c] $\mu = 3 \times 10^{10}$ N m^{-2}.

because of the assumption of uniform slip, it only indicates the region of maximum slip release, as confirmed by results of inversions performed dividing the 20 s fault into 2 × 2 subfaults. If the aspect ratio of the uniform-slip 20 s fault is fixed to 2, optimal parameters (including seismic moment) and costs do not change noticeably for A, and remain practically unchanged for B; along-dip fault width increases to match the aspect ratio.

The total seismic moment of models A and B, computed for $\mu = 3 \times 10^{10}$ Pa, agrees with results from long-period and surface wave data. The seismic moment distribution among the different subevents is, however, different from that found of Giardini (1993), as moments released on the 20 s and 40 s faults of A and B seem underestimated. We have run inversions after fixing the aspect ratio of the 40 s fault up to 3, and the aspect ratio of the 20 s fault up to 2, but no relevant change in the moment distribution has been obtained. Similar conclusions have been reached after dividing the 0 s fault into three along-strike subfaults and the 20 s fault into 2 × 2 subfaults. Discrepancies in the moment distribution might be consequence of reactivation of the 0 s fault during the subsequent events, and/or to small-sized heterogeneities in slip distribution.

The 20 s fault proposed by Pantosti & Valensise (1990, 1993) (a fault dipping 60°–70° towards the northeast, somewhat an extension of the fault related to the 0 s subevent) accounts for the SGM surface fractures but is not consistent with levelling data from line 82 and the southernmost part of line 81 (this work and Pingue *et al.* 1993). Westaway & Jackson (1987) tested values of dip other than 20° for the northeast-dipping nodal plane (namely 2°, 40° and 60°) using teleseismic records, and obtained a much worse comparison among synthetic and observed *P* and *SH* waves at stations MNT and POO with respect to 20°. Even if focal mechanisms by Westaway & Jackson (1987) are not used here to constrain model parameters of the 20 s subevent, it is interesting to note the full consistency between focal planes of the 20 s subevent obtained by Westaway & Jackson (1987) and fault parameters obtained by our unconstrained coseismic displacement inversion.

Palaeoseismological studies carried out along the Marzano-Carpineta and San Gregorio Magno scarps (D'Addenzio *et al.* 1991; Pantosti *et al.* 1993a) showed evidence for the occurrence, on two separated fault sections, of earthquakes similar to the 1980 one during the past 10 000 yr. Stated uncertainties in earthquake timings are in the range 700–2000 yr in the northern segment, and in the range 850–8500 yr in the southern one (D'Addenzio *et al.* 1991; Pantosti *et al.* 1993a, Table 1). Model B is not able to account for the SGM surface ruptures. Trying to overcome this difficulty, we have tested the possible existence of a minor shallow fourth

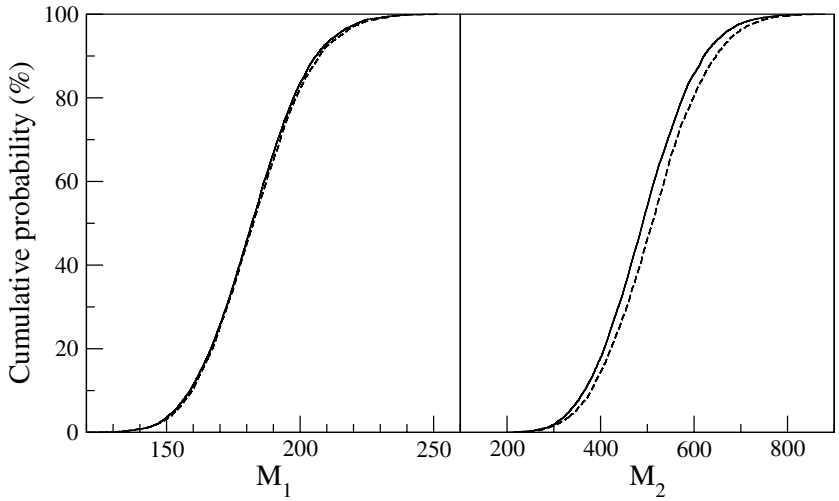

Figure 8. Bootstrap cumulative distribution (per cent probability) for M_1 (left) and M_2 (right). The starting point for the inversions is best-fit A (dashed line), and best-fit B (solid line).

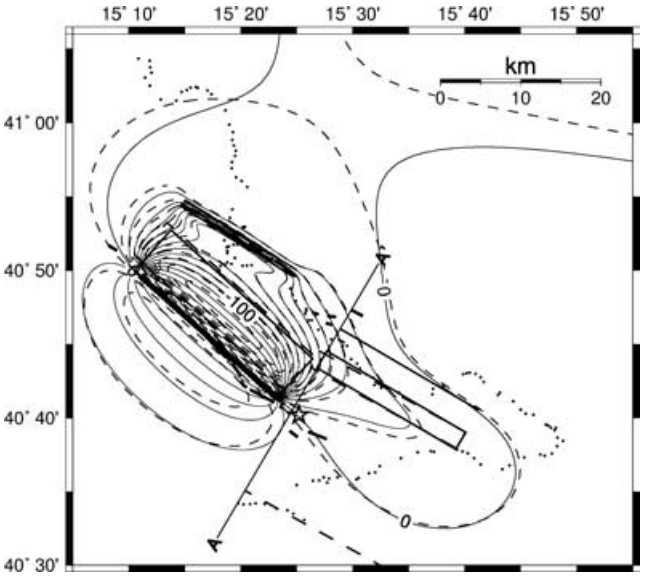

Figure 9. Surface projection of the faults of best-fit A (dashed lines) and B (solid lines) after minimizing M_1 and contour lines of surface vertical displacements (A, dashed; B, solid). The contour step is 10 cm. Star, location of the 1996 ($M_L = 4.9$) earthquake (Cocco *et al.* 1999); AA′, trace of the vertical section in Fig. 11.

Table 3. Velocity and density profile used to test the effects of vertical heterogeneities.

Depth (km)	V_P (m s^{-1})	V_S (m s^{-1})	Density (kg m^{-3})
0.0	2270	1280	2100
3.0	5320	2990	2500
7.0	6030	3390	2750
10.0	6280	3530	2800
20.0	6540	3670	2900
31.0	8000	4600	3300

rupture close to SGM, as already suggested by Westaway (1993) from strong motion records (mainly at BRI station). Also Bernard & Zollo (1989) noticed that the occurrence of a secondary faulting process, within 2 s earlier than the 20-s fault, is reconcilable with strong motion records. We have inverted all levelling data, fixing most parameters of the 40 s fault to reduce the huge number of free parameters. Parameters of the fourth fault have been constrained from the SGM surface fractures (strike $= -15° \pm 5°$, dip $= 60°$, depth of the upper side $\leq$2 km; fault trace centre in a 28 km^2 area including fractures). With respect to B, M_1 cost decreases from 208 to 195 when considering all data, and from 65 to 54 when considering only benchmarks 1–35 and 107–142. Computed uplifts and observations for benchmarks 1–35 and 107–142 are shown in Fig. 10. Minima are not as well defined (i.e. larger) as in B, but parameters of the 0, 20 and 40 s faults are similar to B. The fourth fault is separated from the 0 s fault, is very shallow (upper side approaches the surface), small ($L \simeq 3.5$ km and $W \simeq 6.5$ km) and located close to the SGM eastern rupture (Fig. 1 and, for more details, Pantosti & Valensise 1990, Fig. 4), consistently with the suggestion by Pantosti & Valensise (1990) that the westernmost SGM rupture (along the contact between sediments and limestone) would be driven by pre-existing structural discontinuities. Fault location and cost decrease are intriguing, but we cannot state that the fourth fault really exists, lacking levelling data coverage in the SGM area.

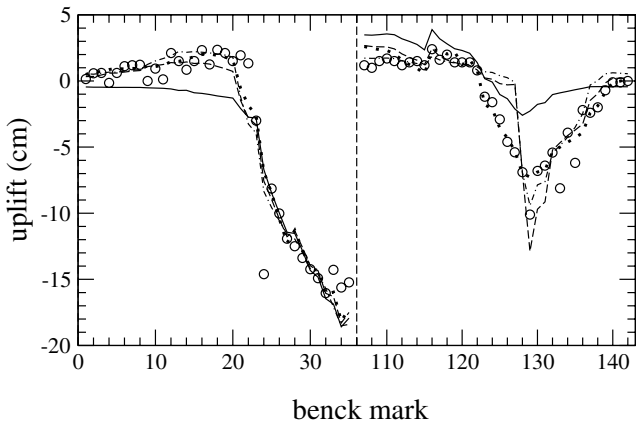

Figure 10. Computed uplifts: solid line, fault model obtained optimizing the Pantosti & Valensise (1990) model with respect to benchmark uplifts and dividing the 20 s fault into four subfaults to relax the uniform slip assumption; dashed line, fault model obtained optimizing the Bernard & Zollo (1989) model with respect to benchmark uplifts and assuming a 20 s fault composed of a shallower steeper subfault and a deeper subhorizontal subfault; dot-dashed line, fault model obtained optimizing the Pingue & De Natale (1993) model with respect to benchmark uplifts; dotted line, four-fault model of this work. Observations (circles) for benchmarks 1–35 and 107–142.

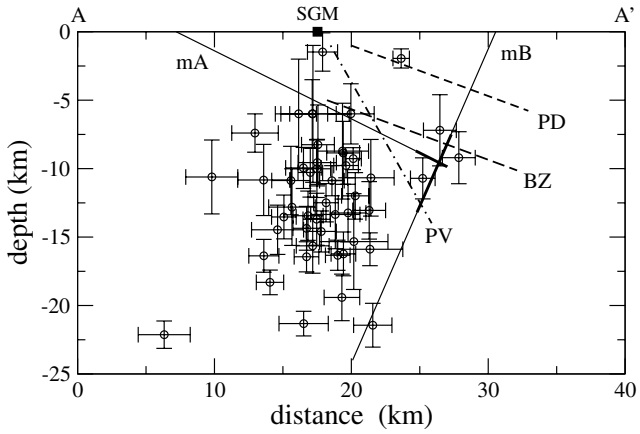

Figure 11. Projection of aftershocks localized southeast of the AA′ trace in Fig. 9 on a vertical N31E cross-section cutting across the San Gregorio Magno area and 20 s fault profiles. SGM, San Gregorio Magno fractures; mA, best-fit model A (fault plane, thin line; effectively slipped area, thick line); mB, best-fit model B (fault plane, thin line; effectively slipped area, thick line); BZ, Bernard & Zollo (1989); PD, Pingue & De Natale (1993); PV, Pantosti & Valensise (1990). Aftershocks are located in the hangingwall block of model B and in the footwall block of all the other models.

A strong earthquake hit an area almost perfectly overlapping that of the 1980 event in 1694 (e.g. Pantosti *et al.* 1993b, Fig. 8). It has been considered the penultimate earthquake on the so-called Irpinia fault (e.g. Serva 1981), but no geological record of the 1694 earthquake has been found in the trenches excavated along the 1980 ruptures (Pantosti *et al.* 1993a,b). As a consequence, Pantosti *et al.* (1993b) suggested that the fault responsible for the 1694 earthquake was similar to, but longer than, the 40 s fault of the 1980 earthquake, and Nostro *et al.* (1997) suggested that the 40 s subevent was a reactivation of a fault segment of the 1694 earthquake. The 20 s B fault is approximately aligned with the 40 s fault and with the surface ruptures reported in Blumetti *et al.* (2002). Thus the 20 s subevent, if really associated with model B, might be due to reactivation of

the southernmost part of the fault related to the 1694 earthquake, as a repetition of its deepest rupture, supporting the existence of a graben-like capable fault system in the area. The western side would have been the origin of the 0-s subevent (and possibly a further minor event close to SGM). The eastern side would have been the origin of both the 40 s and the 20 s subevents.

9 CONCLUSIONS

Although the complex 1980 Campania-Lucania earthquake has been widely investigated in the past using different data sets, the so-called 20 s subevent is controversial, and very different models have been assumed in subsequent literature about, for example, static and dynamic stress triggering and post-seismic deformation. Our statistical analysis of levelling data indicates that the vertical displacement pattern of southernmost benchmarks, although small, strongly supports a model similar to that of Bernard & Zollo (1989) against the other ones. However, a deep northeast-dipping subhorizontal fault is neither more nor less statistically favourable than a southwest steeply dipping fault. This latter model, which is more consistent with southern aftershock distribution, has never been proposed before and suggests that the 20 s subevent could be interpreted as the repetition of the deepest southern rupture of the 1694 earthquake.

ACKNOWLEDGMENTS

Figures have been generated using open-source software (GMT, Wessel & Smith 1998, and Grace). We are grateful to C. Cimoroni for help during the initial stage of this work. Computational support by Laboratori Nazionali del Gran Sasso (INFN) and Consorzio di Ricerca del Gran Sasso is also acknowledged. We are grateful to the Editor and two reviewers for useful comments.

REFERENCES

Amato, A. & Selvaggi, G., 1993. Aftershock location and P-velocity structure in the epicentral region of the 1980 Irpinia earthquake, *Ann. Geofis.*, **XXXVI,** 3–15.

Amoruso, A., Crescentini, L. & Scarpa, R., 1998. Inversion of source parameters from near- and far- field observations: an application to the 1915 Fucino earthquake, central Apennines, Italy, *J. geophys. Res.*, **103,** 29 989–29 999.

Amoruso, A., Crescentini, L. & Scarpa, R., 2002. Source parameters of the 1908 Messina Straits, Italy, earthquake from geodetic and seismic data, *J. geophys. Res.*, **107,** doi:10.1029/2001JB000434.

Arca, S. & Marchioni, A., 1983. I movimenti verticali del suolo nelle zone della Campania e della Basilicata interessate dal sisma del novembre 1980, *Boll. Geod. Sci. Affini*, **42,** 126–135.

Armigliato, A. & Tinti, S., 2003. Influence of topography on coseismic displacements induced by the Friuli 1976 and the Irpinia 1980 earthquakes (Italy) analyzed through a two-dimensional hybrid model, *J. geophys. Res.*, **108,** doi:10.1029/2002JB002027.

Arnadottir, T. & Segall, P., 1994. 1989 Loma Prieta earthquake imaged from inversions of geodetic data, *J. geophys. Res.*, **99,** 21 835–21 855.

Arnadottir, T., Segall, P. & Matthews, M., 1992. Resolving the discrepancy between geodetic and seismic fault models for the 1989 Loma Prieta, California, earthquake, *Bull. seism. Soc. Am.*, **82,** 2248–2255.

Benz, H.M., Chouet, B.A., Dawson, P.B., Lahr, J.C., Page, R.A. & Hole, J., 1996. Three-dimensional P and S wave velocity structure of Redoubt volcano, Alaska, *J. geophys. Res.*, **101,** 8111–8128.

Bernard, P. & Zollo, A., 1989. The Irpinia 1980 earthquake: Detailed analysis of a complex normal faulting, *J. geophys. Res.*, **94,** 1631–1647.

Blumetti, A.M., Esposito, E., Ferreli, L., Michetti, A.M., Porfido, S., Serva, L. & Vittori, E., 2002. Ground effects of the 1980 Irpinia earthquake revisited: evidence for surface faulting near Muro Lucano, in *Large Scale Vertical Movements and Related Gravitational Process, Studi Geologici Camerti, Special Issue*, eds Dramis, F., Farabollini, P. & Molini, P.

Cervelli, P., Murray, M.H., Segall, P., Aoki, Y. & Kato, T., 2001. Estimating source parameters from deformation data, with an application to the March 1997 earthquake swarm off the Izu Peninsula, Japan, *J. geophys. Res.*, **106,** 11 217–11 238.

Cocco, M. & Pacor, F., 1993a. Space-time evolution of the rupture process from the inversion of strong-motion waveforms, *Ann. Geofis.*, **XXXVI,** 109–130.

Cocco, M. & Pacor, F., 1993b. The rupture process of the 1980 Irpinia, Italy, earthquake from the inversion of strong motion waveforms, *Tectonophysics*, **218,** 157–177.

Cocco, M. et al, 1999. The April 1996 Irpinia seismic sequence: evidence for fault interaction, *J. Seismol.*, **3,** 105–117.

Cotecchia, V., Monterisi, L. & Salvemini, A., 1986. Effects of the November 23, 1980 earthquake on the Conza della Campania dam and on its supplemental structures, in *Proceedings of the International Symposium on Engineering Geology Problems in Seismic Areas*, Vol. 4, pp. 363–392, ed. Cotecchia V., Geologia Applicata e Idrogeologia, Bari.

D'Addenzio, G., Pantosti, D. & Valensise, G., 1991. Paleoearthquakes along the Irpinia Fault at Pantano di San Gregorio Magno (Southern Italy), *Il Quaternario*, **4,** 121–136.

Dalla Via, G., De Natale, G., Troise, C., Pingue, F., Obrizzo, F., Riva, R. & Sabadini, R., 2003. First evidence of post-seismic deformation in the central Mediterranean: crustal viscoelastic relaxation in the area of the 1980 Irpinia earthquake (Southern Italy), *Geophys. J. Int.*, **154,** F9–F14.

De Natale, G., Pingue, F. & Scarpa, R., 1988. Seismic and ground deformation monitoring in the seismogenic region of the southern Apennines, Italy, *Tectonophysics*, **152,** 165–178.

Giardini, D., 1993. Teleseismic observations of the November 23 1980, Irpinia earthquake, *Ann. Geofis.*, **XXXVI,** 17–25.

Ingber, L., 1993. Simulated annealing: practice versus theory, *Math. Comput. Modell.*, **18,** 29–57.

Ingber, L. & Rosen, B., 1992. Genetic algorithms and very fast simulated reannealing: a comparison, *Math. Comput. Modell.*, **16,** 87–100.

Kissling, E., Ellsworth, W.L., Eberhart-Phillips, D. & Kradolfer, U., 1994. Initial reference models in local earthquake tomography, *J. geophys. Res.*, **99,** 19 625–19 646.

Lee, W.H.K. & Valdes, C.M., 1985. *HYPO71PC: a Personal Computer Version of the HYPO71 Earthquake Location Program*, US Geological Survey Open File Report 85–749, US Geological Survey, Reston, VA.

Murray, M.H., Marshall, G.A., Lisowski, M. & Stein, R., 1996. The 1992 M = 7 Cape Mendocino, California, earthquake: coseismic deformation at the south end of the Cascadia megathrust, *J. geophys. Res.*, **101,** 17 707–17 725.

Nostro, C., Cocco, M. & Belardinelli, M.E., 1997. Static stress change in extensional regimes: an application to southern Apennines (Italy), *J. geophys. Res.*, **87,** 234–248.

Okada, Y., 1985. Surface deformation due to shear and tensile faults in a half-space, *Bull. seism. Soc. Am.*, **75,** 1135–1154.

Pantosti, D. & Valensise, G., 1990. Faulting mechanism and complexity of the November 23, 1980, Campania-Lucania earthquake, inferred from surface observations, *J. geophys. Res.*, **95,** 15 319–15 341.

Pantosti, D. & Valensise, G., 1993. Source geometry and long-term behavior of the 1980, Irpinia earthquake fault based on field geologic observations, *Ann. Geofis.*, **XXXVI,** 41–49.

Pantosti, D., D'Addenzio, G. & Cinti, F.R., 1993a. Paleoseismological evidence of repeated large earthquakes along the 1980 Irpinia earthquake fault, *Ann. Geofis.*, **XXXVI,** 231–330.

Pantosti, D., Schwartz, D.P. & Valensise, G., 1993b. Paleoseismology along the 1980 surface rupture of the Irpinia fault: implications for earthquake recurrence in the southern Apennines, Italy, *J. geophys. Res.*, **98,** 6561–6577.

Pingue, F. & De Natale, G., 1993. Fault mechanism of the 40 seconds subevent of the 1980 Irpinia (southern Italy) earthquake from levelling data, *Geophys. Res. Lett.*, **20,** 911–914.

Pingue, F., De Natale, G. & Briole, P., 1993. Modeling of the 1980 Irpinia earthquake source: constraints from geodetic data, *Ann. Geofis.*, **XXXVI,** 27–40.

Pollitz, F., Burgmann, R. & Segall, P., 1998. Joint estimation of afterslip rate and postseismic relaxation following the 1989 Loma Prieta earthquake, *J. geophys. Res.*, **103,** 26 955–26 992.

Press, W.H., Teukolsky, S.A., Vetterling, W.T. & Flannery, B.P., 1992. *Numerical Recipes in C: the Art of Scientific Computing*, 2nd edn, Cambridge University Press, New York.

Salichon, J., Delouis, B., Lundgren, P., Giardini, D., Costantini, M. & Rosen, P., 2003. Joint inversion of broadband teleseismic and interferometric synthetic aperture radar (InSAR) data for the slip history of the Mw = 7.7, Nazca ridge (Peru) earthquake of 12 November 1996, *J. geophys. Res.*, **108,** 2085, doi:10.1029/2001JB000913.

Serva, L., 1981. Il terremoto del 1694 in Irpinia e Basilicata, in *Proceedings of the Annual Meeting of the Progetto Finalizzato Geodinamica on Sismicità dell'Italia: Stato delle Conoscenze Scientifiche e Qualità della Normativa Simica*, pp. 183–208, Consiglio Nazionale delle Ricerche, Rome.

Vaccari, F., Harabaglia, P., Suhadolc, P. & Panza, G.F., 1993. The Irpinia (Italy) 1980 earthquake: waveform modelling of accelerometric data and macroseismic considerations, *Ann. Geofis.*, **XXXVI,** 93–108.

Wang, R., Martin, F.L. & Roth, F., 2003. Computation of deformation induced by earthquakes in a multi-layered elastic crust- FORTRAN programs EDGRN/EDCMP, *Comput. Geosci.*, **29,** 195–207.

Wessel, P. & Smith, W.H.F., 1998. New, improved version of the Generic Mapping Tools released, *EOS, Trans. Am. geophys. Un.*, **79,** 579.

Westaway, R., 1993. Fault rupture geometry for the 1980 Irpinia earthquake: a working hypothesis, *Ann. Geofis.*, **XXXVI,** 51–69.

Westaway, R.W.C. & Jackson, J.A., 1984. Surface faulting in the southern Italy Campania-Basilicata earthquake of 23 November 1980, *Nature*, **312,** 436–438.

Westaway, R.W.C. & Jackson, J.A., 1987. The earthquake of 1980 November 23 in Campania-Basilicata (southern Italy), *Geophys. J. R. astr. Soc.*, **90,** 375–443.